The ASBM-SA turbulence closure: Taking advantage of structure-based modeling in current engineering CFD codes

Constantinos Panagiotou, Stavros Kassinos, Bertrand Aupoix

The ASBM-SA turbulence closure: Taking advantage of structure-based modeling in current engineering CFD codes

C.F. Panagiotou [a], S.C. Kassinos [a,*], B. Aupoix [b]

[a] *Computational Sciences Laboratory, UCY-CompSci, Department of Mechanical & Manufacturing Engineering, University of Cyprus, 75 Kallipoleos, Nicosia 1678, Cyprus*
[b] *ONERA, The French Aerospace Lab, F-31055 Toulouse, France*

Structure-based turbulence models (SBM) carry information about the turbulence structure that is needed for the prediction of complex non-equilibrium flows. SBM have been successfully used to predict a number of canonical flows, yet their adoption rate in engineering practice has been relatively low, mainly because of their departure from standard closure formulations, which hinders easy implementa-tion in existing codes. Here, we demonstrate the coupling between the Algebraic Structure-Based Model (ASBM) and the one-equation Spalart–Allmaras (SA) model, which provides an easy route to bringing structure information in engineering turbulence closures. As the ASBM requires correct predictions of two turbulence scales, which are not taken into account in the SA model, Bradshaw relations and numer-ical optimizations are used to provide the turbulent kinetic energy and dissipation rate. Attention is paid to the robustness and accuracy of the hybrid model, showing encouraging results for a number of simple test cases. An ASBM module in Fortran-90 is provided along with the present paper in order to facilitate the testing of the model by interested readers.

1. Introduction

Currently, the computation of turbulent flows in industrial design and engineering applications relies heavily on the use of simple turbulence models in the Reynolds-Averaged Navier Stokes (RANS) equations. This has been a long-standing trend and is sustained by practical considerations. For example, the computational resources needed by Direct Numerical Simulations, and even by Large-Eddy Simulations, are still excessive for routine use in many engineering applications.

The class of RANS models most often used in engineering applications is that of Eddy Viscosity Models (EVM). One of the most popular EVM is the Spalart–Allmaras (SA) one-equation model (Spalart and Allmaras, 1994). The SA model is often favored by practicing engineers because it exhibits superior robustness, low CPU time requirements and substantially lower sensitivity to grid resolution compared to two-equation models. On the other hand, one has to recognize that, despite its computational and implementational attractiveness, the eddy viscosity assumption is also the source of some of the most important performance limitations. For example, like other EVM, the SA model fails to capture important flow features, such as turbulence anisotropy or the effects of mean or system rotation.

The widespread use of EVM in engineering practice, despite their inherent limitations, is sustained by the lack of clearly superior alternatives that would justify the extra computational complexity required. For example, efforts to circumvent the limitations of the eddy viscosity assumption usually proceed along one of three paths. One path is that of Differential Reynolds Stress Models (DRSM), where the closure carries the Reynolds Stress Transport (RST) equations. DRSM closures allow the prediction of stress anisotropy, account for history effects on the anisotropy, and afford improved handling of rotational and curvature effects. However, robustness issues and performance inconsistencies have prevented this class of models from penetrating further into the mainstream of engineering practice. For example, a number of large European research projects were aimed at introducing DRSM models in industrial codes (FLOMANIA and ATAAC), but did not lead to a significant change in industrial CFD practice. A second common choice is to use one of the Explicit Algebraic Reynolds Stress Models (EARSM), which are based on a weak equilibrium assumption that leads to a constitutive equation between the turbulence stresses and the mean deformation field. In addition, EARSM involve the transport of two turbulence scales. The anisotropy equilibrium assumption that is inherent to EARSM has been a known source of performance limitations in complex

* Corresponding author.
E-mail address: kassinos@ucy.ac.cy (S.C. Kassinos).

non-equilibrium flows. A third option is resort to Nonlinear Eddy Viscosity Models (NLEVM), where the stress–strain relation is extended with additional terms. NLEVM and EARSM models can be made to show sensitivity to curvature and rotation, but cannot handle consistently complex rotational effects.

A common feature of the classical closure approaches described so far is the assumption that all key information about the turbulence is contained in the scales of the turbulence and in the turbulence stress tensor. However, one should consider that the turbulent stresses contain information only about the componentality of the turbulence, i.e. about the directions in which the turbulence fluctuations associated with large-scale eddies are most energetic. Thus, traditional closures do not take into account the morphology of the energy-containing eddies. Yet, eddies tend to organize spatially the fluctuating motion in their vicinity. In doing so, they eliminate gradients of fluctuation fields in some directions (those in which the spatial extent of the structure is significant) and enhance gradients in other directions (those in which the extent of the structure is small). Thus, associated with each eddy are local axes of dependence and independence that determine the dimensionality of the local turbulence structure. This structure dimensionality information is complementary to the componentality information contained in the Reynolds stresses, and as Kassinos and Reynolds (1994) and Kassinos et al. (2001) have shown it is dynamically important.

Reynolds and Kassinos identified this common limitation of classical closures and introduced an alternative modeling approach, the Structure-Based Turbulence Models (SBM), which today provide a promising route for devising improved RANS turbulence closures. SBM can be envisioned in two complementary ways. The first is to use directly the structure tensors that characterize the morphology of the turbulence. The transport of these tensors is governed by exact partial differential equations that have been derived and this provides the starting point for differential SBMs, such as the Q-model (Poroseva et al., 2002). In general, differential SBMs involve a large number of transport equations, which can be unattractive for routine engineering computations. Hence, a second way is to assume that the turbulence can be mimicked by ensembles of simplified structures, hypothetical 2D eddies, whose axis of independence is given by an eddy-axis vector. The orientation of the eddy-axis can be obtained through model equations, either differential or algebraic. These eddies are 2D, but they can be jetal 2D–1C (motion only along the eddy-axis), vortical 2D–2C (motion in planes normal to the eddy-axis) or helical 2D–3C (correlated motion along and normal to the eddy axis). Averaging over ensembles of eddies produces statistical quantities representative of the field and allows one to relate the Reynolds stress tensor to the statistics of the turbulence structure (Kassinos and Reynolds, 1994). The Algebraic Structure-Based Model (ASBM) (Kassinos et al., 2006; Langer and Reynolds, 2003) is an engineering structure-based turbulence model that follows this second approach. It is a fully realizable two-equation structure-aware model that provides the full Reynolds stress tensor.

In the ASBM, the eddy-axis is obtained through an algebraic equation that takes into account asymptotic rapid distortion theory (RDT) limits. Under RDT, the governing equations are linearized by neglecting products of turbulent fluctuations. This linearization is based on the assumption that the turbulence does not have time to interact with itself because the eddy turnover timescale is much longer than that of the mean distortion. Near solid boundaries, the model is sensitized to the wall-blocking effect through an elliptic relaxation equation that is based on the physical argument that eddies must be realigned parallel to the wall as the wall is approached. While the ASBM comes with its own transport equations for the turbulence scales (notably the Large-Scale Enstrophy Equation LSE) (Reynolds et al., 2002), it has recently been successfully coupled with the scale equations of popular Eddy-Viscosity Models (EVM), such as the v^2–f (Kalitzin et al., 2004), the k–ε–ϕ–α (Benton, 2011) and the k–ω models (Kassinos et al., 2006; Aupoix et al., 2009; Kalitzin et al., 2004).

Inspired by these considerations, here we present the coupling of the ASBM with the one-equation SA model. The motivation is that the hybrid ASBM-SA model can potentially combine the numerical robustness and stability of the SA model along with the deeper physical content of the ASBM that ensures full realizability. Because the coupling can be added to existing SA implementations with minimal additional effort, such an approach could provide immediate access to ASBM technology in engineering codes. Thus, the main objectives of this work are (a) to describe the coupling of the ASBM and SA closures, (b) to outline the implementation of ASBM-SA model in our solver and evaluate its computational characteristics, such as numerical stability, and speed of convergence, and (c) to evaluate the performance of the model in a number of standard benchmark cases.

2. ASBM modeling

The ASBM belongs to the family of Structure-Based turbulence Models (SBM) that are designed to include information about the morphology of the energy-containing turbulence eddies. ASBM has been built as an engineering simplification to more complex differential structure-based turbulence models (Kassinos et al., 2000; Poroseva et al., 2002), and requires two turbulence scales and the mean velocity gradients as inputs. Given these inputs, it uses algebraic relations to return the normalized structure tensors, including the Reynolds stresses, as output.

2.1. Structure parametrization

The fundamental idea behind the algebraic structure representation in ASBM is that any three-dimensional three-component (3D–3C) turbulent field can be constructed by the superposition of an ensemble of simpler 2D–3C fields representing individual eddies. Thus, individual eddies can be envisioned as building blocks that are used in ensembles to represent complex turbulence fields. Individual eddies can differ in character according to their componentality (C) and dimensionality (D). Averaging over an ensemble of eddies yields an algebraic constitutive equation that relates the normalized Reynolds stress tensor r_{ij} to the other structure parameters of the ensemble

$$r_{ij} = \frac{1}{2}(1-\phi)(\delta_{ij}-a_{ij}) + \phi a_{ij} + (1-\phi)\chi\left[\frac{e^-}{2}\delta_{ij} - \frac{e^+}{2}a_{ij} - b_{ij} + [ab]_{ij}\right] - \gamma_k(\epsilon_{ipr}a_{pj} + \epsilon_{jpr}a_{pi})\left\{\frac{(1-\chi e^-)}{2}\delta_{kr} + \chi b_{kr} - \chi a_{kn}b_{nr}\right\}, \quad (1)$$

where we have used

$$e^{\pm} = 1 \pm a_{nm}b_{mn}, \quad [ab]_{ij} = a_{in}b_{nj} + a_{jn}b_{ni}. \quad (2)$$

To compute the Reynolds stress tensor one has to know the structure parameters that appear on the R.H.S. of Eq. (1), namely the eddy-axis tensor a_{ij}, the jetal parameter ϕ, the helical parameter γ, the flattening tensor b_{ij} and flattening scalar χ. These are obtained through model functions that are based on the asymptotic states produced by the RDT of homogeneous turbulence and adjusted for the effects of weak deformation and wall-proximity, where appropriate. A brief description of these structure parameters and of the model functions used to compute them is given below and in greater detail in (Langer and Reynolds, 2003; Aupoix et al., 2009).

2.1.1. Eddy-axis tensor

The unit eddy-axis vector a_i describes the orientation of individual eddies. The eddy-axis tensor a_{ij} is the energy-weighted, ensemble-averaged direction cosine tensor of the eddies,

$$a_{ij} = A_{ij}/q^2 \qquad A_{ij} = \langle u^2 a_i a_j \rangle, \tag{3}$$

where the angled brackets denote averaging, $u^2 = u_i u_i$ is the magnitude of the fluctuating velocity and $q^2 = \langle u^2 \rangle$ is twice the turbulent kinetic energy. In differential SBM, the evolution of a_{ij} is based on the transport equation for a material line in homogeneous turbulence. In the ASBM, a_{ij} is obtained by following the weak-equilibrium procedure of Rodi (1976), where it is assumed that variations in A_{ij} are due to variations in q^2 only, while variations in a_{ij} are neglected. Thus,

$$\frac{dA_{ij}}{dt} \approx 2a_{ij}(\mathcal{P} - \varepsilon), \tag{4}$$

where $\mathcal{P}$ and ε are the production and dissipation rates of the turbulent kinetic energy. Furthermore, the algebraic procedure is split into two steps, based on the assumption that the effects of irrotational mean deformation and mean rotation on the eddy axis tensor can be decomposed. This splitting is justified by the observation that the orientation of the eddy-axis must be computed in the analysis frame where the flow is in equilibrium or very close to it. This is typically a rotating frame. The eddy axis is computed with no reference to the frame rotation, as it is only kinematically rotated by it (Kassinos and Reynolds, 1994; Haire and Reynolds, 2003). The two evaluation steps are summarized next.

The irrotational contribution is calculated using the implicit algebraic expression

$$a^s_{ij} = \frac{\delta_{ij}}{3} + \tau \frac{S^*_{ik}a^s_{kj} + S^*_{jk}a^s_{ki} - \frac{2}{3}|Sa^s|\delta_{ij}}{a_o + 2\sqrt{a_1^2 + \tau^2 S^*_{kp}S^*_{kq}a^s_{pq}}}, \tag{5}$$

where τ is a turbulent time scale, $S^*_{ij} = S_{ij} - S_{kk}\delta_{ij}/3$ is the anisotropic part of the mean strain rate tensor S_{ij}, and $|Sa_s| = S^*_{pq}a^s_{qp}$. Here, $a_o = 1.4$ and $a_1 = (2.1 - a_o)/2$ are "slow" parameters whose values were determined by considering the initial growth rate of the Reynolds stress anisotropy when $S\tau$ is very small. Moreover, these parameters were optimized simultaneously with other model constants to ensure the model satisfies a canonical boundary-layer state.

Next, mean rotation effects are included through a rotation operator H_{ij} that is applied to a^s_{ij} in order to yield the final homogeneous eddy-axis tensor

$$a_{ij} = H_{ik}H_{jm}a^s_{km}, \tag{6}$$

where H_{ij} is the rotational transformation tensor, given by

$$H_{ij} = \delta_{ij} + \alpha_1 \frac{\Omega_{ij}}{\sqrt{\Omega_{st}\Omega_{st}}} + \alpha_2 \frac{\Omega_{ip}\Omega_{pj}}{\Omega_{st}\Omega_{st}}. \tag{7}$$

Here, Ω_{ij} is mean rotation tensor. The requirement that H_{ij} obeys the orthonormality conditions $H_{ip}H_{jp} = \delta_{ij}$ and $H_{pi}H_{pj} = \delta_{ij}$ enforces a dependence between the two coefficients α_1 and α_2, namely

$$\alpha_1 = \sqrt{2\alpha_2 - \alpha_2^2/2}. \tag{8}$$

Matching the RDT limiting states under the combined action of mean plane strain and rotation determines α_2 (Haire and Reynolds, 2003)

$$\alpha_2 = \begin{cases} 2 - 2\sqrt{\frac{1}{2}(1 + \sqrt{1 - r})} & \text{if } r \leqslant 1 \\ 2 - 2\sqrt{\frac{1}{2}(1 - \sqrt{1 - 1/r})} & \text{if } r \geqslant 1, \end{cases}$$

where $r = (a_{pq}\Omega_{qr}S^*_{rp})/(S^*_{kn}S^*_{nm}a_{mk})$.

2.1.2. Jetal parameter

Motion around the eddy-axis is called vortical, whereas the motion aligned to it is called jetal. The eddy jetal parameter $0 \leqslant \phi \leq 1$ represents the fraction of the energy in the jetal mode. Of course, the energy fraction in the vortical mode is given by $1 - \phi$. In the ASBM, it is assumed that homogeneous isotropic turbulence is composed entirely of vortical eddies. The vortical character of the turbulence ($\phi = 0$) is preserved by rapid irrotational strain, but in the presence of mean rotation the jetal component is activated.

2.1.3. Helical parameter

Under rapid irrotational strain the turbulence is assumed to be vortical. Jetal turbulence results from the breaking of reflectional symmetry (Kassinos and Reynolds, 1994; Kassinos et al., 2001) caused by mean or frame rotation. Furthermore, in the presence of mean shear, the vortical and jetal components of motion are correlated. In the ASBM, the correlation between the vortical and jetal components is related to the stropholysis vector γ_k. The stropholysis vector is zero for purely vortical or purely jetal turbulence, leading to

$$\gamma = \beta\sqrt{\frac{2\phi(1-\phi)}{1+\chi}}, \quad \gamma_k = \gamma\frac{\Omega^T_k}{\sqrt{\Omega^T_s\Omega^T_s}}, \tag{9}$$

where γ is the helical parameter, β is a parameter indicative of the degree of correlation between fluctuating velocities at different directions. Ω^T_k is the total rotation vector given by the sum of the frame and the mean rotation vector. χ is the eddy flattening parameter introduced next.

2.1.4. Eddy flattening

If the motion is not axisymmetric around the eddy, the eddy is called flattened. This asymmetry occurs when rotation is present and is incorporated in the model through a scalar, called flattening parameter χ, and a tensor, called the flattening tensor b_{ij}. The flattening tensor b_{ij} is modeled in terms of the mean and frame vorticity vectors Ω_i and Ω^f_i,

$$b_{ij} = \frac{\Omega^*_i\Omega^*_j}{|\Omega^{*2}|}, \quad \Omega^*_i = \Omega_i + C_b\Omega^f_i. \tag{10}$$

To capture the correct sign of the secondary shear stress for the case of shear with streamwise frame rotation, C_b is set equal to -1. Thus, b_{ij} is a frame-dependent parameter, sensitized to the particular frame choice.

2.2. Computation of the structure scalars

Completion of the homogeneous formulation of the ASBM requires the specification of the scalar structure parameters ϕ, β, γ and χ. In the general case, these are defined in a three-dimensional space in terms of

$$\eta_m = \sqrt{\frac{\hat{\Omega}^2_m}{\hat{S}^2}} \quad \eta_f = \eta_m - \text{sign}(X)\sqrt{\frac{\hat{\Omega}^2_T}{\hat{S}^2}} \quad a^2 = a_{ij}a_{ji}, \tag{11}$$

where, $\hat{\Omega}^2_m = -a_{ij}\Omega_{ik}\Omega_{kj}$, $\hat{\Omega}^2_T = -a_{ij}\Omega^T_{ik}\Omega^T_{kj}$, $\hat{S}^2 = a_{ij}S^*_{ik}S^*_{kj}$, and $X = a_{ij}\Omega^T_{ik}S^*_{kj}$. Functional forms for the scalar structure parameters, such as $\phi = \phi(\eta_m, \eta_f, a^2)$, and $\beta = \beta(\eta_m, \eta_f, a^2)$, are chosen with reference to RDT limiting states, while interpolation functions are chosen to bridge between these limiting RDT states and isotropy. The details of the functional forms can be found in (Langer and Reynolds, 2003) and are also given in Appendix A.

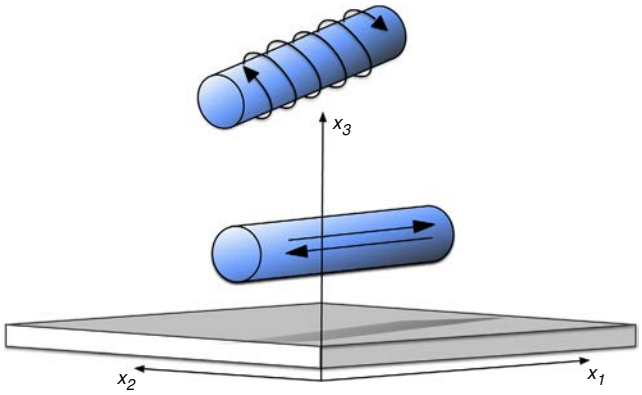

Fig. 1. An eddy becomes jetalized due to the blocking effect of a solid boundary.

2.3. Near-wall effects

In the ASBM, it is assumed that as a solid boundary is approached, the turbulence eddies are forced by wall blocking to become parallel to the plane of the wall, as shown in the diagram of Fig. 1. At the same time, the eddies become jetal because of the blocking on the wall-normal velocity component. As described below, the parametrization of the turbulence structure is adjusted for these wall-proximity effects through an elliptic blocking procedure.

2.3.1. Blocking parameter

The blocking scalar parameter Φ provides a measure of the proximity to the wall. This parameter is computed through an elliptic relaxation equation

$$L^2 \frac{\partial^2 \Phi}{\partial x_j^2} = \Phi, \quad L = 0.17 \max\left(\frac{k^{3/2}}{\varepsilon}, 80.0\sqrt[4]{\frac{\nu^3}{\varepsilon}}\right), \tag{12}$$

where k, ε are the turbulent kinetic energy and the dissipation rate respectively.

2.3.2. Blockage tensor

The blockage tensor is computed from the scalar blocking parameter

$$B_{ij} = \begin{cases} \frac{\Phi_{,i}\Phi_{,j}}{\Phi_{,k}\Phi_{,k}}\Phi, & \text{if } \Phi_{,k}\Phi_{,k} > 0 \\ 0, & \text{if } \Phi_{,k}\Phi_{,k} = 0, \end{cases} \tag{13}$$

and gives the strength and the direction of the wall projection. Thus, depending on the distance from the wall as measured through Φ, the eddies are partially projected onto a plane parallel to the wall, through the operation

$$a_{ij} = P_{ik}P_{jl}a^h_{kl}, \tag{14}$$

where the eddy projection tensor P_{ij} is given by

$$P_{ik} = \frac{(\delta_{ik} - B_{ik})}{D_a}, \quad D_a^2 = 1 - (2 - B_{kk})a^h_{mn}B_{nm}. \tag{15}$$

Note that the eddies are renormalized during the operation so that the eddy axis tensor is maintained as the energy-weighted direction cosine tensor of unit trace. The "jetalization" of the eddies due to the preferential blocking of the wall-normal velocity component is accomplished through the blocking of the jetal and helical scalar eddy parameters

$$\phi = 1 + (\phi^h - 1)(1 - B_{kk})^2, \quad \gamma = \gamma^h(1 - B_{kk}). \tag{16}$$

Additional details on the ASBM formulation can be found in Appendix A, while a Fortran-90 module containing the ASBM implementation is also provided (ASBM, 2014).

3. Coupling with the SA model

The Spalart–Allmaras (SA) closure is a one-equation turbulence model developed primarily for application in aerodynamics, but which has been successfully applied in a wider range of flows. The main limitation of SA (and any other one-equation model) is that it does not provide of a complete set of turbulence scales. On the other hand, the ASBM closure relies on the availability of suitable turbulence scales and this was the key stumbling block in trying to couple the ASBM and SA closures.

3.1. The Bradshaw hypothesis

As early as the 1940s, a number of authors (Dryden, 1948) had made the observation that in attached boundary layer flows the turbulent shear stress can be assumed to be approximately proportional to the turbulent kinetic energy and proposed simple models based on this approximation

$$|-\overline{uv}|/k = a_1. \tag{17}$$

Later Bradshaw et al. (1967) elaborated this approach further and used it as the basis for constructing a one-equation turbulence closure based on the assumption of a constant a_1, and as a result Eq. (17) is often referred to as 'the Bradshaw relation'. This relation is the starting point for coupling of the SA closure to the ASBM because it provides the framework for extracting the two turbulence scales needed by the ASBM from the SA closure.

Early attempts to use Eq. (17) for the construction of one-equation closures were based on the assumption of a constant a_1 throughout the flowfield. However, DNS and experimental data indicate that a_1 is not a constant in the near wall regime, neither in the viscous sublayer of the turbulent boundary layer, nor at the edge of the boundary layer, as indicated by Fares and Schroder (2005) and Nagano et al. (2000). In their work, Nagano et al. provided a variable a_1 for the Bradshaw relation through the use of Boussineq approximation,

$$\frac{|-\overline{uv}|}{k} = a_1 = \frac{\nu_T}{k}\frac{\partial u_t}{\partial y_n}, \tag{18}$$

where u_t is the tangential component of the mean velocity and y_n is the normal to the wall component of the local coordinate system,

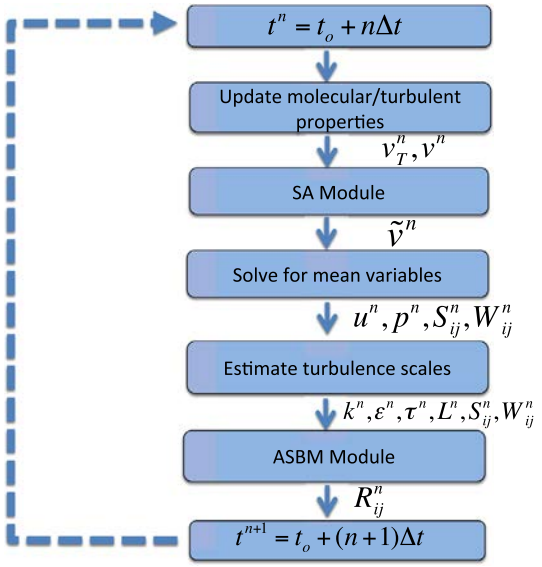

Fig. 2. Schematic description of the structure of the coupling algorithm.

and where the turbulence structure parameter is assumed to have the functional form

$$a_1 = \sqrt{C_\mu f_a}. \tag{19}$$

Here, the role of the model function f_a is to account for the variation of a_1 in the viscous sublayer and the edge of the boundary layer.

3.2. Adaptation to the Spalart–Allmaras model

Traditionally, the Bradshaw hypothesis has been used as the starting point for transforming k–ε closures to one equation models. Here, our objective is to use the same phenomenology in order to extract the turbulence scales (k and ε) from the SA one-equation closure. Hence, we next require that the eddy viscosity as defined in the context of the SA closure (Spalart and Allmaras, 1994),

$$\nu_T = f_{v1}\tilde{\nu}, \tag{20}$$

be consistent with the eddy viscosity arising in the low Reynolds number k–ε model, namely

$$\nu_T = C_\mu f_\mu R, \quad R = \frac{k^2}{\varepsilon}, \tag{21}$$

which yields the relation

$$f_{v1}\tilde{\nu} = C_\mu f_\mu R = \nu_T. \tag{22}$$

Using Eqs. (19) and (22) in (18), allows the turbulent kinetic energy to be expressed in the form

$$k = \tilde{\nu}\sqrt{\frac{f_{v1}}{C_\mu}} f_{\chi_{sa}} S, \quad f_{\chi_{sa}} = \sqrt{\frac{f_{v1}}{f_a}}, \tag{23}$$

where the strain invariant $S = \sqrt{2S_{ij}S_{ij}}$ has been used in place of the velocity gradient $\partial u_t/\partial y_n$ for generality. The function $f_{\chi_{sa}}$ accounts for the variation of the turbulence structure parameter in both the viscous sublayer and the boundary layer edge and in general is depended on the SA parameter χ_{sa} and on C_μ. Based on numerical optimizations the functional form

$$f_{\chi_{sa}} = 1 + C_{\chi_{sa}}^{0.8}, \quad C_{\chi_{sa}} = \sqrt{C_\mu^2 + 1/(1+\chi_{sa})^2}, \quad C_\mu = 0.09, \tag{24}$$

has been adopted (Rahman et al., 2011).

3.2.1. Specification of the effective strain contributions

Two important limitations of Eq. (23) is that it does not hold true in regions where S tends to zero and it does not adequately account for rotational effects. To overcome these limitations, and thus extend the range of applicability of the coupled closure, a modified strain rate $S_{\chi_{sa}}$ is introduced in Eq. (23), given by

$$S_{\chi_{sa}} = \sqrt{\tilde{S}^2 + \tilde{S}_a^2}. \tag{25}$$

Here, $\tilde{S}$ represents an effective strain rate corrected for rotational effects, while $\tilde{S}_a$ provides an effective strain contribution in regions where S tends to zero.

Following the approach of Rahman et al. (2011), the effective strain contributions are evaluated according to

$$\tilde{S} = f_k\left(S - \frac{|n_1| - n_1}{C_T}\right), \tag{26}$$

with

$$n_1 = S - W, \quad f_k = 1 - \frac{\tilde{f}_a}{C_T}\sqrt{\max(1 - Ra, 0)},$$
$$Ra = |W/S|, \quad \tilde{f}_a = 1 - \exp\left(-\frac{\mu_T}{36\mu}\right), \tag{27}$$

where $W = \sqrt{2\Omega_{ij}\Omega_{ij}}$ and $C_T = 2.0$. In Eq. (26), the term inside the parenthesis considers the region where $Ra > 1$, such as in the vortex core, whereas function f_k accounts for $Ra < 1$ and ensures a smooth transition between the two regions. The second contribution to the modified strain rate, which provides a correction away from the wall, is given by

$$\tilde{S}_a = \frac{2C_{\chi_{sa}}\tilde{f}_a}{3\nu}\left(\frac{\sqrt{\tilde{u}_i^2/2}}{1 + \mu_T/\mu}\right)^2, \tag{28}$$

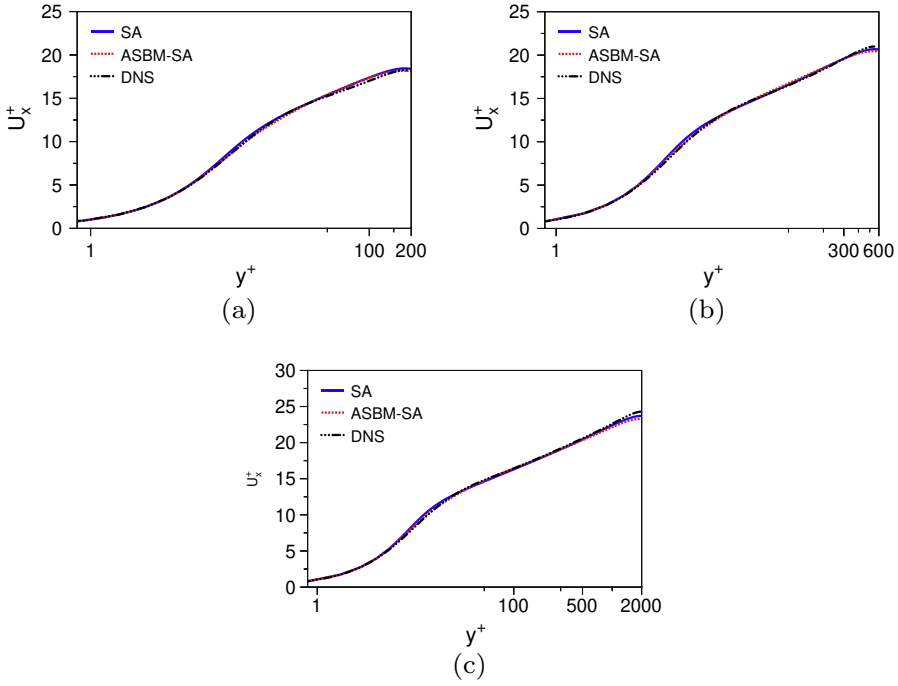

Fig. 3. Fully-developed turbulent channel flow at (a) $Re_\tau = 180$ (b) $Re_\tau = 550$ and (c) $Re_\tau = 2000$. Model predictions (lines) for the streamwise mean velocity are compared to the DNS results (symbols) (Alamo and Jimenez, 2003; Hoyas and Jimenez, 2006).

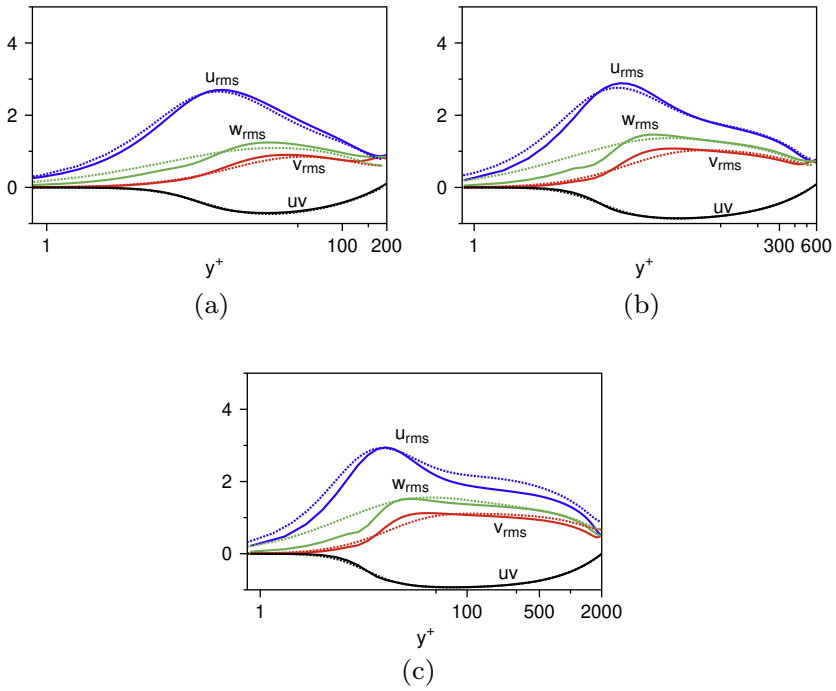

Fig. 4. Fully-developed turbulent channel flow at (a) $Re_\tau = 180$ (b) $Re_\tau = 550$ and (c) $Re_\tau = 2000$. The predictions of the ASBM-SA model (solid lines) for the streamwise intensities are compared to the DNS results (dashed lines) (Alamo and Jimenez, 2003; Hoyas and Jimenez, 2006).

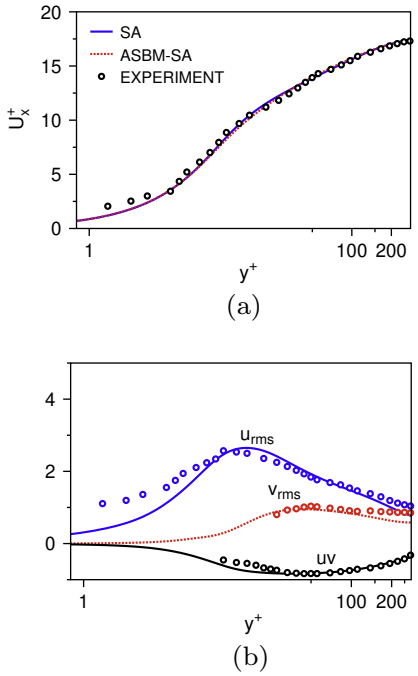

Fig. 5. Turbulent boundary layer at $Re_\delta = 4772$. SA and ASBM-SA model predictions (lines) for (a) the streamwise mean velocity and ASBM-SA model predictions (lines) for (b) the rms and shear stresses. Comparison is made to the experimental values of Loureiro et al. (2007), shown as symbols.

where $C_{\chi_{sa}}$ is given in Eq. (24) and $\tilde{u}_i$ is the mean velocity vector relative to the wall. Summarizing, k is obtained from the equation

$$k = \tilde{\nu} f_{\chi_{sa}} \sqrt{\frac{f_{v1}}{C_\mu}} S_{\chi_{sa}}, \tag{29}$$

along with the set of relations (24)–(28).

3.2.2. Consistent computation of the dissipation rate

In addition, a consistent evaluation of the dissipation rate ε is necessary in order to ensure realizable time and length scales. Following similar arguments as for the kinetic energy case (Rahman et al., 2011), an algebraic expression for the reduced dissipation rate $\tilde{\varepsilon}$ is adopted

$$\tilde{\varepsilon} = f_{v1}^{1.3} \tilde{\nu} S_{\chi_{sa}}^2, \tag{30}$$

where the exponent of f_{v1} is chosen through numerical optimizations.

Solid wall corrections. At a solid wall, both k and $\tilde{\varepsilon}$ tend to zero, but the vanishing of the reduced dissipation leads to numerical singularities and thus an additional correction is needed. The remedy is the addition of a term ε_w, which signifies the equality between the wall dissipation rate to the viscous-diffusion rate (Patel et al., 1985; Rahman et al., 2011), given by

$$\varepsilon_w = 2A_e \nu \left(\frac{\partial u_t}{\partial y_n}\right)_w^2 \approx 2A_e \nu S_{\chi_{sa}}^2, \tag{31}$$

where ν is the kinematic viscosity of the fluid. Experimental and DNS data for channel flows and flow over a flat plate indicate a range for A_e between $0.05 < A_e < 0.11$. In the current computations, $A_e = C_\mu = 0.09$ is adopted.

Summing all parts that contribute to the dissipation rate yields the final modeling expression

$$\varepsilon = \sqrt{\varepsilon_w^2 + \tilde{\varepsilon}^2}. \tag{32}$$

3.3. Determination of the ASBM time scale

The coupling of ASBM to the SA closure is completed by using Eqs. (29) and (32) to obtain k and ε respectively, which are then used for computing the turbulence time and length scales through the expressions (Lien et al., 1998),

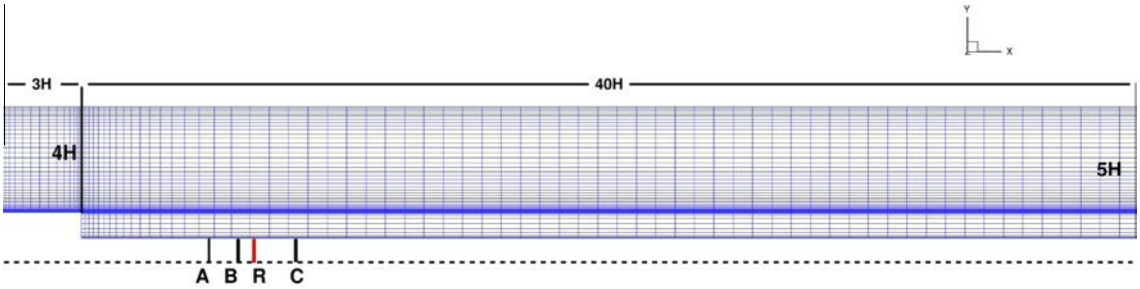

Fig. 6. Geometry and grid design for RANS computations of turbulent flow over a backward facing step at inlet $Re_h = 5100$. The domain inlet is located at a distance of $3H$ upstream of the step corner, while the outlet is at a distance $40H$ downstream the corner. The ratio between inlet-step height is 4. Data is extracted at two stations located within the re-circulation region (A, B) and one station located at the recovery region (C). The location of the experimental reattachment point (R) is also shown.

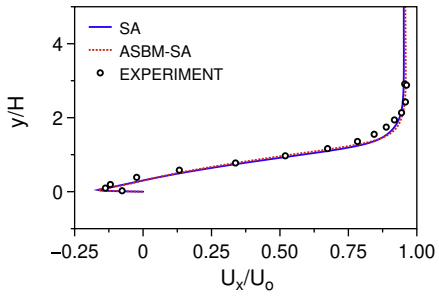

(a) $x/H = 4$

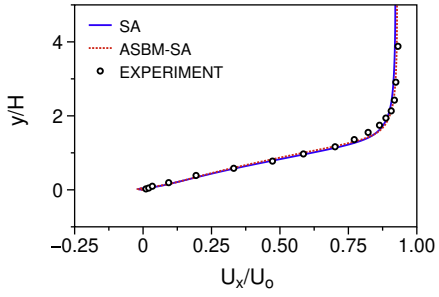

(b) $x/H = 6$

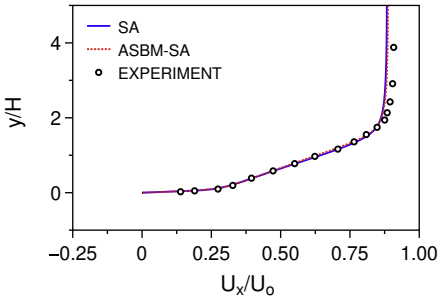

(c) $x/H = 10$

Fig. 7. Turbulent flow over a backward facing step at $Re_h = 5100$. Model predictions for the streamwise mean velocity at streamwise locations: (a) $x/h = 4$, (b) $x/h = 6$ and (c) $x/h = 10$. Comparison is made to the experiments of Jovic and Driver (1995), shown as symbols.

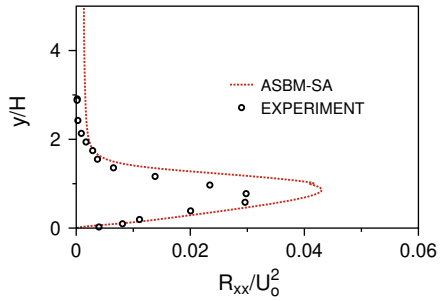

(a) $x/H = 4$

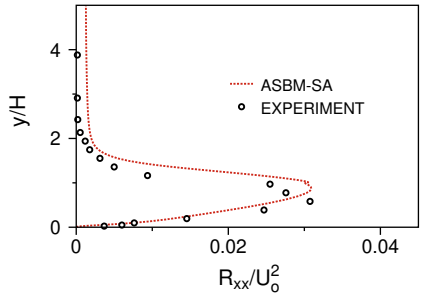

(b) $x/H = 6$

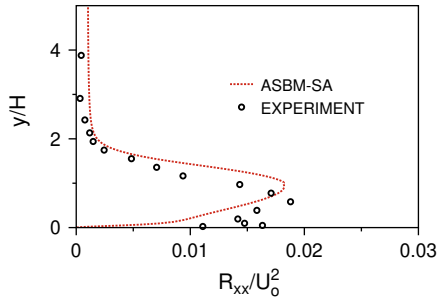

(c) $x/H = 10$

Fig. 8. Turbulent flow over a backward facing step at $Re_h = 5100$. ASBM-SA model predictions for the normalized streamwise Reynolds stress (R_{xx}/U_o^2) at different streamwise locations: (a) $x/h = 4$, (b) $x/h = 6$ and (c) $x/h = 10$. Comparison is made to the experiments of Jovic and Driver (1995), shown as symbols.

$$\tau = \max\left(\frac{k}{\varepsilon}, C_T\sqrt{\frac{\nu}{\varepsilon}}\right), \quad L = C_L \max\left(\frac{k^{3/2}}{\varepsilon}, C_n\left(\frac{\nu^3}{\varepsilon}\right)^{1/4}\right), \tag{33}$$

where $C_L = 0.17$, $C_n = 80.0$, τ is the time scale and L is the characteristic length scale. For near-wall turbulence, a lower bound based on the Kolmogorov scales is imposed on the time and length scales. This procedure ensures proper near-wall behavior of the turbulence scales. Fig. 2 demonstrates a schematic description of the numerical procedure that was followed in the current work.

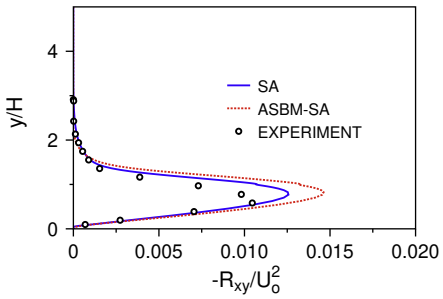

(a) $x/H = 4$

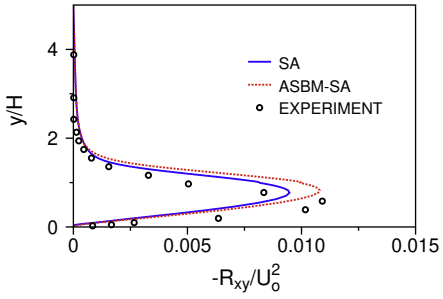

(b) $x/H = 6$

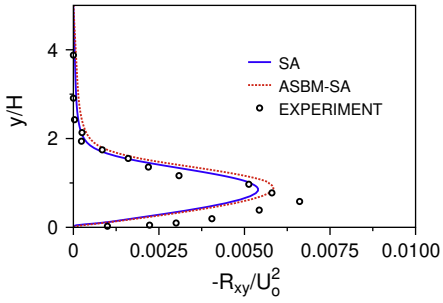

(c) $x/H = 10$

Fig. 9. Turbulent flow over a backward facing step at $Re_h = 5100$. SA and ASBM-SA predictions for the normalized turbulent shear stress ($-R_{xy}/U_o^2$) at three x-stations: (a) $x/h = 4$, (b) $x/h = 6$ and (c) $x/h = 10$. Comparison is made to the experiments of Jovic and Driver (1995), shown as symbols.

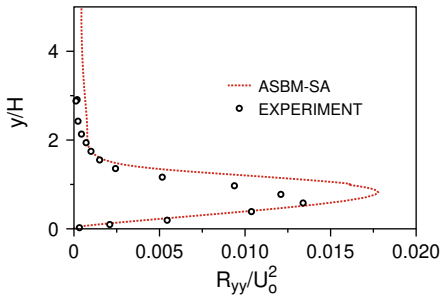

(a) $x/H = 4$

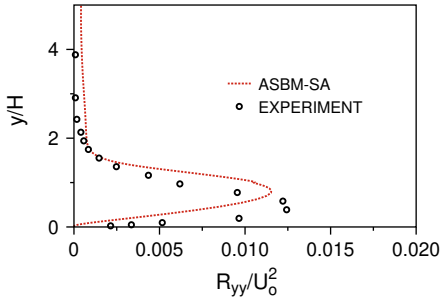

(b) $x/H = 6$

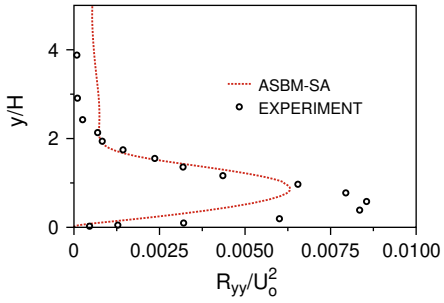

(c) $x/H = 10$

Fig. 10. Turbulent flow over a backward facing step at $Re_h = 5100$. ASBM-SA predictions for the transverse Reynolds stress (R_{yy}/U_o^2) at three x-stations: (a) $x/h = 4$, (b) $x/h = 6$ and (c) $x/h = 10$. Comparison is made to the experiments of Jovic and Driver (1995), shown as symbols.

4. Computations

In order to test the efficiency and performance of the proposed ASBM-SA model, we consider a series of two-dimensional flows, namely a fully-developed channel flow, a turbulent boundary layer over a flat plate, a backward-facing step, an asymmetric diffuser and a smooth steep hill. The model is validated against DNS and experimental data and compared to the standard SA model. In all cases, the computations were repeated on progressively finer grids till a grid independent solution was achieved. An unstructured, nodal-based finite-volume code called CDP that has been developed at the Center of Turbulence Research (Stanford/NASA) is used as a general platform. For the discretization of the diffusive and advection terms in both the mean and turbulent transport equations, a second-order accurate centered-difference scheme with skewness corrections has been used. The coupling of the transport equations is done through a fractional-step method, while a Crank–Nicholson scheme is used for time integration. Details of the code have been described extensively in (Ham et al., 2006).

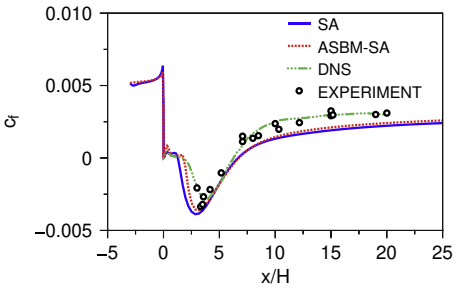

Fig. 11. SA and ASBM-SA model predictions for the skin-friction coefficient at the bottom wall. Comparison is made to experiments of Jovic and Driver (1995) and the DNS of Le et al. (1997).

4.1. Fully-developed channel flow

Computations are carried out for fully-developed turbulent channel flow at a Reynolds numbers $Re_\tau = 180$, $Re_\tau = 550$ and $Re_\tau = 2000$, based on the channel half-height δ and friction

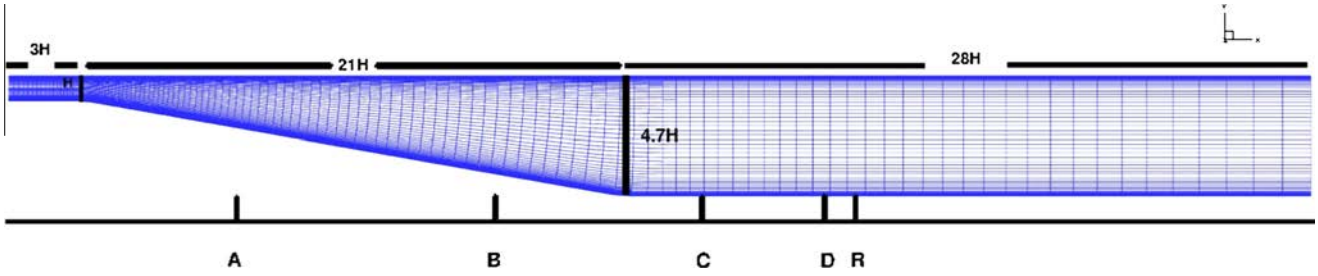

Fig. 12. Geometry and mesh details for RANS computations of turbulent flow in an asymmetry diffuser. The domain inlet is located at a distance of 3*H* upstream the point at the beginning of the expansion region, while the outlet is at a distance 49*H* downstream that point. The expansion domain is 21*H* long at the streamwise direction, yielding an expansion ratio of 4.7. Data is extracted at four stations located within the re-circulation region. The re-attachment point(R) is also shown.

velocity u_τ. The profiles are compared to the DNS data of Alamo and Jimenez (2003) and Hoyas and Jimenez (2006). The flow is maintained by a uniform mean pressure gradient imposed along the streamwise direction x. No-slip boundary conditions are applied at the top and bottom walls and periodic conditions along the other two directions. Computations are carried on a $1 \times 105 \times 1$ nonuniform grid based on the grid independence test and in order to ensure proper near-wall resolution, the first cells adjacent to the walls are placed at $y^+ < 1.0$. Results are non-dimensionalized using the friction velocity, as $U_x^+ = U_x/u_\tau$, $u_{rms} = \sqrt{R_{xx}}/u_\tau$, $v_{rms} = \sqrt{R_{yy}}/u_\tau$, $w_{rms} = \sqrt{R_{zz}}/u_\tau$ and $uv = -R_{xy}/u_\tau^2$.

Fig. 3a–c show the mean velocity profile for the low ($\mathrm{Re}_\tau = 180$), the intermediate ($\mathrm{Re}_\tau = 550$) and the high ($\mathrm{Re}_\tau = 2000$) Reynolds number cases, respectively. In all cases, the predictions of both the ASBM-SA and SA models agree well with the DNS data. As shown, in the buffer and log-layer regions ($30 < y^+ < 50$), the ASBM-SA coupling produces a marginal improvement relative to the SA predictions.

Corresponding profiles for the rms quantities are displayed in Fig. 4a–c, where again good agreement of the model predictions with the DNS data is noted. The SA closure cannot provide predictions for the rms turbulence quantities and thus the comparison is made only between the ASBM-SA closure and the DNS results.

4.2. Turbulent boundary layer

Next, we consider the case of a turbulent boundary layer flow over a flat plate, for which many experimental datasets are available. Here, we have chosen to validate the model against the experiments of Loureiro et al. (2007), since these are related to the inlet conditions used later for the 'Witch of Agnesi' case. The Reynolds number is $\mathrm{Re}_\delta = 4772$, based on freestream velocity u_δ and the boundary thickness δ, corresponding to a friction-velocity Reynolds number of $\mathrm{Re}_\tau = 277$. At the inlet, Dirichlet boundary conditions are imposed for $\tilde{\nu}$ and U_i, while zero-flux is used for the other variables. For all flow variables, a penalty condition is applied at the outlet to ensure mass conservation and a zero-flux at the top free surface, while symmetry conditions are used in the spanwise direction. Finally, a no-slip condition is used at the bottom wall. In order to ensure adequate resolution, the cells adjacent to the wall are placed within $y^+ < 0.9$. The computations are carried on a nonuniform grid of size $63 \times 104 \times 1$ in the streamwise, wall-normal and spanwise directions, respectively. The grid is stretched along the wall-normal direction, but kept uniform along the streamwise. Finer grids were also considered, which all converged to the same solutions, indicating grid-independence for our results.

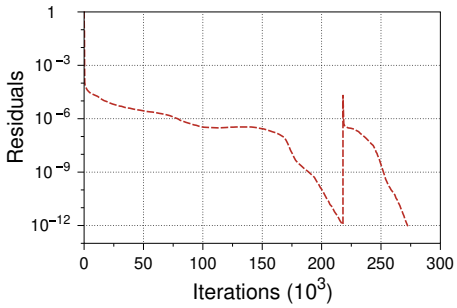

Fig. 13. Time history of the mean velocity residual for the ASBM-SA. The instantaneous jump in the residual levels, indicates the point where the ASBM coupling is turned on.

Fig. 5a highlights the performance of the ASBM-SA closure. In the case of the mean velocity U_x^+, the predictions lie very close to those of the SA model and are in good agreement with the experiments. As shown in Fig. 5b, the ASBM-SA predictions for the rms turbulent fluctuations are in very good agreement with the experimental values for $y^+ > 10$.

4.3. Backward facing step

To ascertain the performance in separated flows, the proposed model is applied to the flow over a backward facing step. This is the simplest benchmark case with flow separation, since the separation point is fixed. Computations are conducted for flow conditions that correspond to the experiment performed by Jovic and Driver (1995) and the DNS computations by Le et al. (1997). At the inlet, a zero-pressure-gradient (ZPG) boundary layer profile is imposed, corresponding to a Reynolds number $\mathrm{Re}_h = 5100$ based on the step size h and the freestream velocity u_o, and taken from an SA computation of a ZPG boundary layer. The same (SA based) inlet profile was used for both the SA and the ASBM-SA computations in order to make the comparison more meaningful. The ratio between the inlet height and the step height is 4. In the current computations, the grid is arranged in two blocks. The upper block (the area above the step) contains a $160 \times 91 \times 1$ nonuniform grid, while the lower one contains a $134 \times 31 \times 1$ nonuniform grid respectively. Both grids are stretched in both the streamwise and the crossflow directions. The grid independence of our results was verified by computing the flow on a finer grid containing an upper block of $161 \times 153 \times 1$ and a lower one of $134 \times 63 \times 1$ and demonstraing that the solution remained unaffected. The maximum distance between the first grid cell and the wall is kept within $y^+ \leqslant 0.75$. Details of the flow geometry and grid design are shown in Fig. 6.

The inlet conditions are specified at a distance of 3*h* upstream of the corner, whereas the outlet boundary conditions are imposed at 40*h* downstream of the corner. The imposed boundary conditions correspond to slip conditions at the top surface of the domain, no-slip conditions at the bottom wall, and periodic conditions in the spanwise direction.

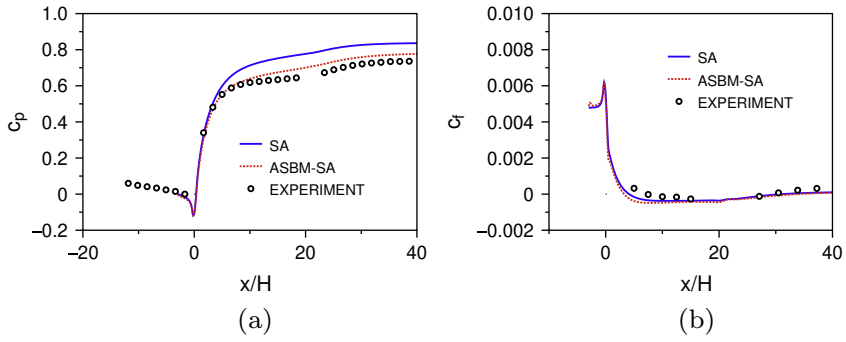

Fig. 14. SA and ASBM-SA model predictions at the bottom wall for (a) the wall static-pressure coefficient and (b) the wall skin-friction coefficient. Comparison is made to the experimental values of Buice and Eaton (2000).

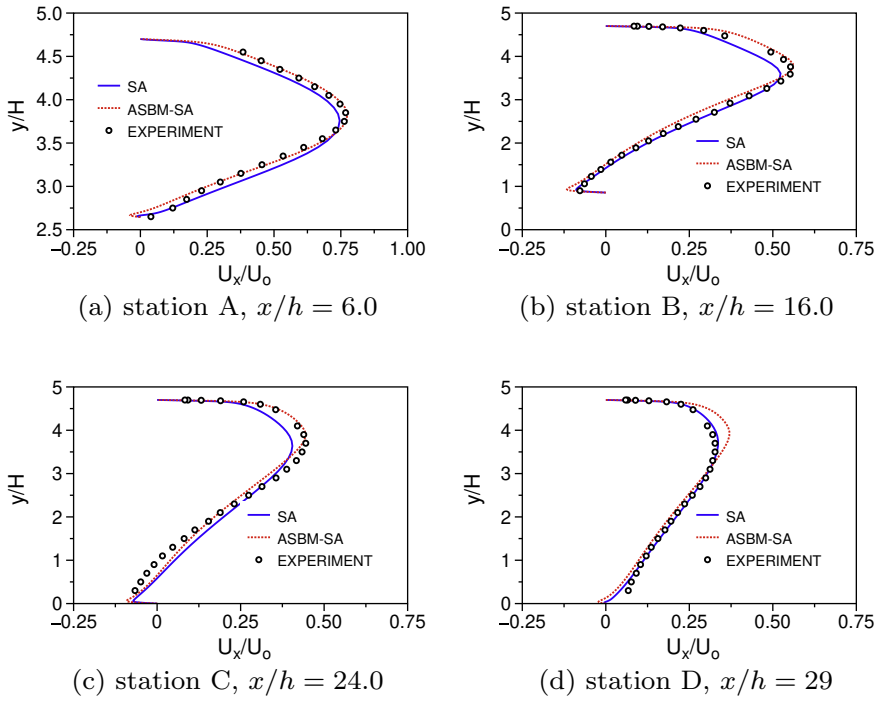

Fig. 15. Turbulent flow over the asymmetry diffuser. Model predictions for the streamwise mean velocity U_x at various x-stations for SA and ASBM-SA closures. Comparison is made to the experimental values of Buice and Eaton (2000).

All the quantities reported are normalized by the step size h and the reference freestream velocity u_o. The distance x/h is measured exactly from the step corner. The streamwise mean velocity profiles at three representative positions are shown in Fig. 7a–c. The first two positions, $x/h = 4$ and $x/h = 6$ are located inside the recirculation region, whereas the third, $x/h = 10$, is within the recovery region. As shown, both the SA and ASBM-SA models capture accurately the profiles in the separation region. In the recovery region, a slight underestimation of the freestream value is observed.

Comparisons for the distributions of Reynolds stress components at the three reference locations are shown in Fig. 8–10. The ASBM-SA closure provides encouraging results in both the recirculation and recovery regions. It captures both the peak magnitudes and the freestream values, proving its sensitivity to the anisotropic nature of this flow. The re-attachment length X_r predicted by DNS is $X_r = 6.39$ in step-height units. Both SA and ASBM-SA predict the same $X_r = 6.51$.

The variation of the skin-friction coefficient C_f with streamwise distance along the bottom wall is shown in Fig. 11. Both the SA and ASBM-SA closures are in reasonable agreement with the experimental and DNS results, but the ASBM-SA produces slightly improved C_f levels in the recirculation bubble and after reattachment.

4.4. Asymmetric diffuser

Steady flow in a two dimensional asymmetric diffuser is considered next. In this type of flow, adverse pressure gradients are generated leading to a large recirculation bubble. The flow conditions are chosen to correspond to the reliable and detailed experimental database of Buice and Eaton (2000). The profile specified at the inlet is obtained from an SA solution for a fully-developed channel flow corresponding to a Reynolds number of Re = 20,000 based on the channel height and the centerline velocity. At the bottom and top walls a no-slip condition is applied, whereas periodic conditions are used in the spanwise direction. Finally, a penalty condition is used at the outlet, ensuring mass conservation. A $148 \times 68 \times 1$ non-uniform grid is used, stretched along the transverse direction so that the $y^+ < 1$ of all grid points adjacent to the walls. Fig. 12 shows details of the computational grid, where the stations marked with letters A through D correspond to the positions

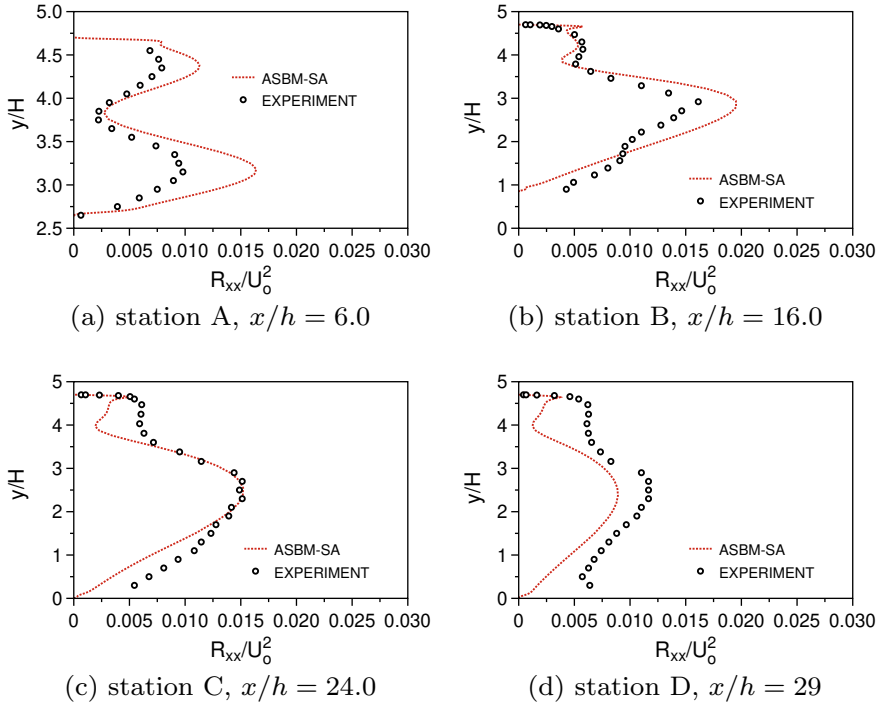

Fig. 16. Model predictions for the streamwise components R_{xx} at various x-stations for SA and ASBM-SA closures. Comparison is made to the experimental values of Buice and Eaton (2000).

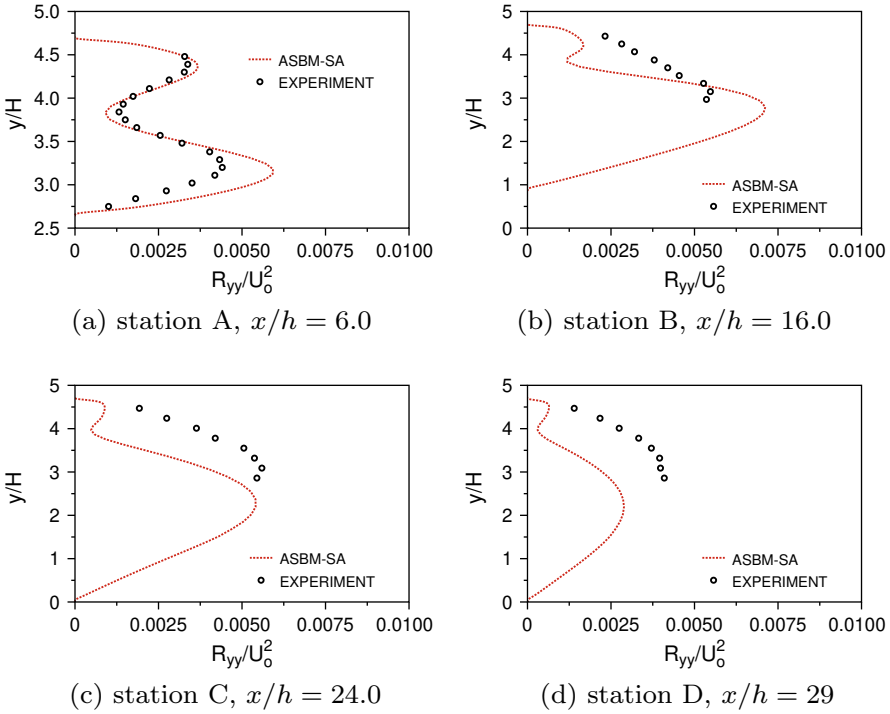

Fig. 17. Model predictions for the streamwise components R_{yy} at various x-stations for SA and ASBM-SA closures. Comparison is made to the experimental values of Buice and Eaton (2000).

$x/h = 6,\ x/h = 16,\ x/h = 24$ and $x/h = 29$ respectively, which are all located inside the recirculation region. Station A roughly corresponds to the experimental flow separation point. Finally, station R corresponds to the location of the experimental re-attachment point, which was located approximately at $x/h = 30$. Comparisons between model predictions and experimental results are done at these locations.

Fig. 13 demonstrates the time development of the maximum velocity residual, ensuring that fully converged, steady solutions are reached. The residual is normalized by its initial value and is given by

$$\text{Res} = \max\left[\frac{V \times \Delta U/\Delta t}{(V \times \Delta U/\Delta t)_o}\right], \quad \Delta U = U^{n+1} - U^n, \tag{34}$$

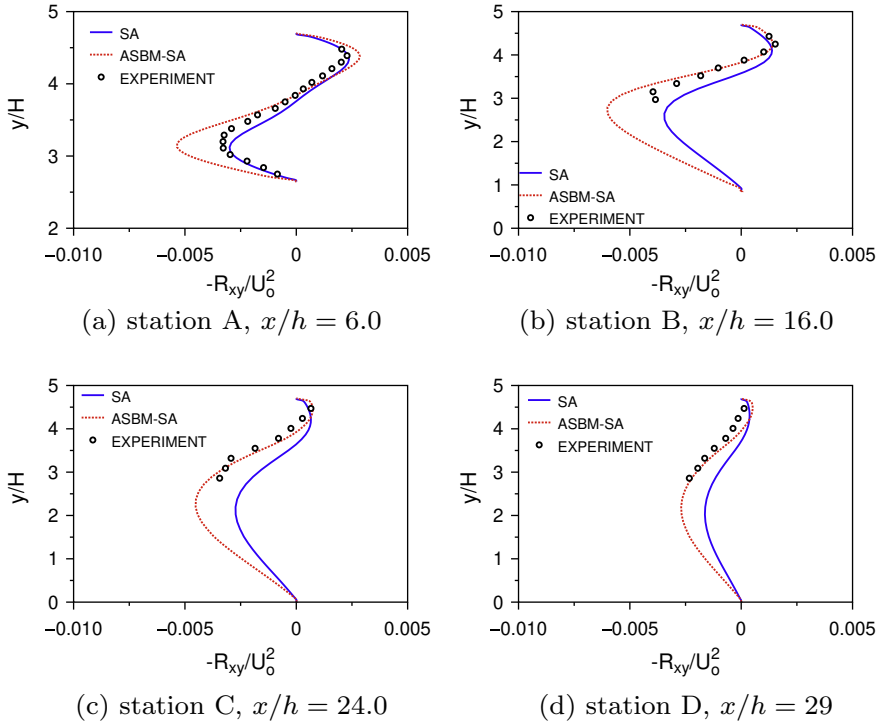

Fig. 18. Model predictions for the shear stress component R_{xy} at various x-stations for SA and ASBM-SA closures. Comparison is made to the experimental values of Buice and Eaton (2000).

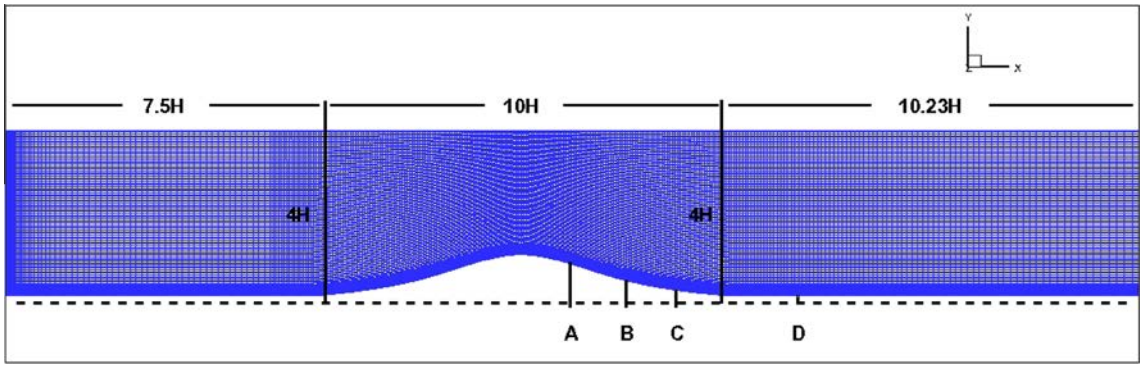

Fig. 19. Geometry and grid design for RANS computations of turbulent flow over the 'Witch of Agnesi Hill' at inlet $\mathrm{Re}_\delta = 4772$. The domain inlet is located at a distance of $12.5H$ from the hilltop, while the outlet is at $15.23H$. The domain height is $4H$. Data is extracted at three stations located within the re-circulation region (A, B, C) and one station located near the experimental re-attachment point.

where n is the number of iteration, Δt is the uniform time step, U is the streamwise mean velocity and V is the volume of the corresponding cell. As shown in Fig. 13, the ASBM-SA model achieves the same final residual levels as the SA closure, an observation that applies to all cases considered in this work.

Both mean and turbulent quantities are normalized by the channel height H and the reference bulk velocity U_o, obtained from the channel simulation. The origin of the x coordinate ($x/h = 0$) is located at the beginning of the expansion section.

Fig. 14 showcases the predictions of the ASBM-SA and SA models for the wall static-pressure coefficient $C_p = (p - p_o)/\frac{1}{2}\rho U_o^2$ and the skin-friction coefficient C_f along the bottom wall. The ASBM-SA closure yields a significant improvement in the prediction of C_p relative to SA, especially after reattachment (see Fig. 14a). The ASBM-SA model correctly predicts both the drop and the subsequent recovery of the pressure, with only a slight overestimation of the C_p near the outlet. This difference between experiments and predictions has also been observed in the LES results of Kaltenbach et al. (1999) The two models produce similar C_f predictions that are in good agreement with the experiments. Based on these skin-friction results, the separation and re-attachment points are predicted by both the SA and ASBM-SA models to be approximately at $x/h = 3.6$ and $x/h = 33.5$ respectively. Thus, both models over-predict the size of the recirculation bubble. These results are consistent with those of DalBello et al. (2005) who has also computed the same case using the SA model. A slight C_f oscillation is observed in the solution of both models at $x/h \approx 20$. This wiggle in the C_f profile is located around the point $x/H = 21$, which is the point where the geometry exhibits a sharp change (end of expansion region). Thus, these oscillations in the C_f profile seem to be associated with the sudden change of the geometry and are most likely caused by the recirculating flow encountering the inclined wall. These disturbances in the C_f profile are also known to be exhibited in the solutions of other RANS models (DalBello et al., 2005).

Fig. 15 shows the predictions for the mean streamwise velocities at the reference stations. As shown, the ASBM-SA predictions

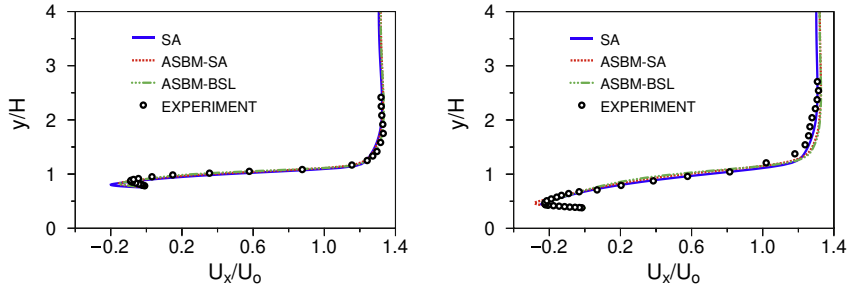

(a) station A, $x/h = 1.25$ (b) station B, $x/h = 2.5$

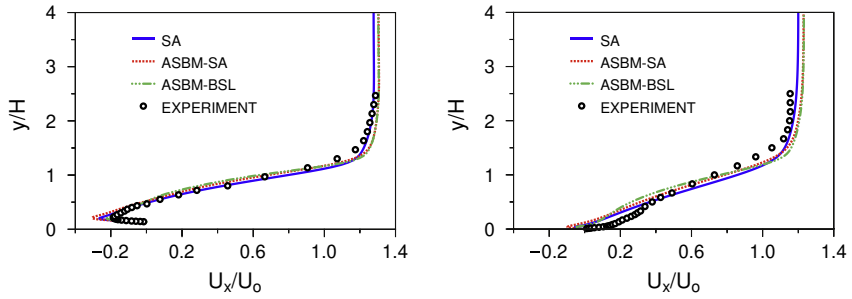

(c) station C, $x/h = 3.75$ (d) station D, $x/h = 6.67$

Fig. 20. Turbulent flow over the 'witch of Agnesi' smooth hill. Model predictions for the streamwise mean velocity U_x at various x-stations for SA and ASBM-SA closures. Comparison is made to experimental values (Loureiro et al., 2007) and the predictions of ASBM-BSL model.

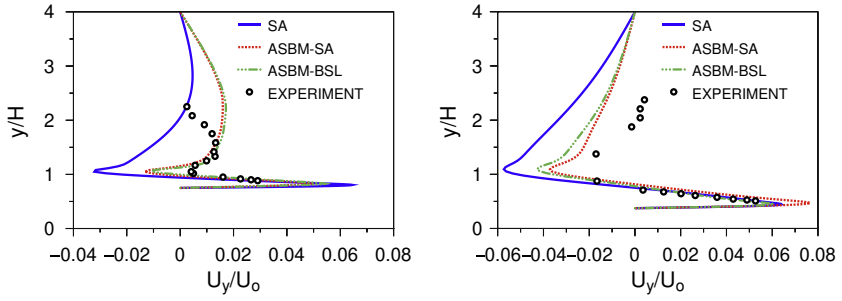

(a) station A, $x/h = 1.25$ (b) station B, $x/h = 2.5$

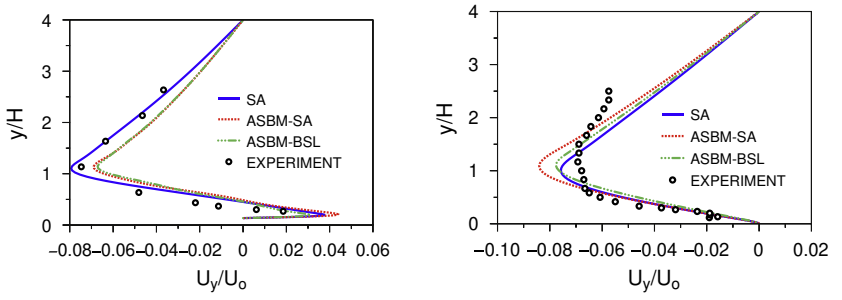

(c) station C, $x/h = 3.75$ (d) station D, $x/h = 6.67$

Fig. 21. Model predictions for the streamwise mean velocity U_y at various x-stations for SA and ASBM-SA closure. Comparison is made to experimental values and the predictions of ASBM-BSL model.

are in better agreement with the experiments than the SA predictions at all stations, except at the last one that is located at the edge of the recirculation region.

Comparisons between the ASBM-SA predictions and the experiments for the diagonal R_{xx} and R_{yy} Reynolds stress components are shown in Figs. 16 and 17 respectively. The closure is in fair agreement with the experiments, capturing the peak levels and saddle points in the profiles. Fig. 18 shows comparison between ASBM-SA predictions and SA for the shear stress component R_{xy}. At the first two stations, ASBM-SA overestimates the near wall peak magnitude at the bottom wall, whereas SA captures the correct magnitudes. At the last two-stations however, the closure recovers and provides better agreement with experiments than the SA closure.

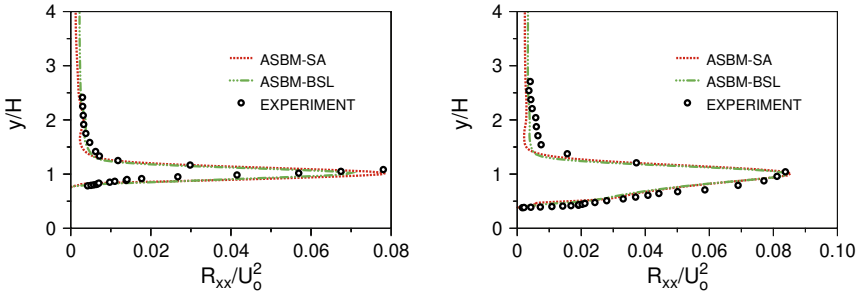

(a) station A, $x/h = 1.25$ (b) station B, $x/h = 2.5$

(c) station C, $x/h = 3.75$ (d) station D, $x/h = 6.67$

Fig. 22. Model predictions for the streamwise Reynolds stress R_{xx} at various x-stations for SA and ASBM-SA closure. Comparison is made to experimental values and the predictions of ASBM-BSL model.

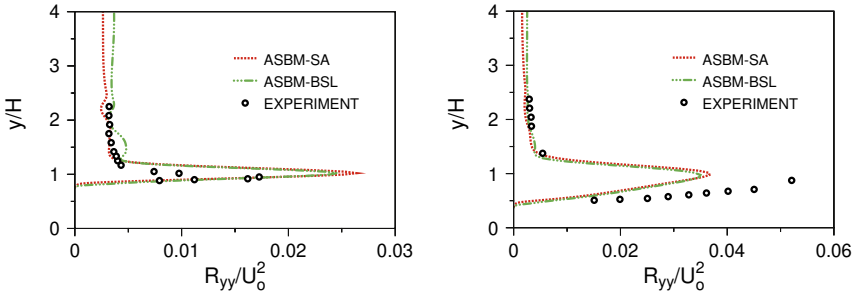

(a) station A, $x/h = 1.25$ (b) station B, $x/h = 2.5$

(c) station C, $x/h = 3.75$ (d) station D, $x/h = 6.67$

Fig. 23. Model predictions for the transverse Reynolds stress R_{yy} at various x-stations for SA and ASBM-SA closure. Comparison is made to experimental values and the predictions of ASBM-BSL model.

4.5. Smooth hill

To further evaluate the model performance in configurations involving flow separation, we consider next a case in which the separation point is not fixed. Thus, the ASBM-SA and SA models are applied to a model complex terrain, specifically to flow over a steep smooth hill. The shape of the hill is defined using a modified 'Witch of Agnesi' profile. Detailed near-wall experimental data (Loureiro et al., 2007) provide a good data set for model validation. For the sake of comparison, additional computations for the same case were performed using the ASBM-BSL model, which is a two-equation hybrid closure that was implemented by us in the same code. We have chosen to compare to this particular closure because it had previously been shown that among ASBM

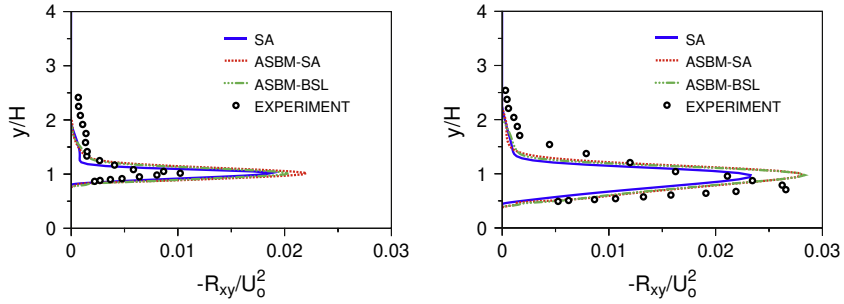

(a) station A, $x/h = 1.25$ (b) station B, $x/h = 2.5$

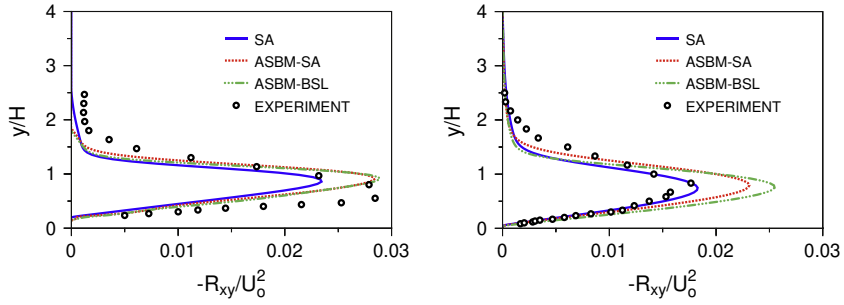

(c) station C, $x/h = 3.75$ (d) station D, $x/h = 6.67$

Fig. 24. Model predictions for the shear stress at various x-stations for SA and ASBM-SA closure. Comparison is made to experimental values and the predictions of ASBM-BSL model.

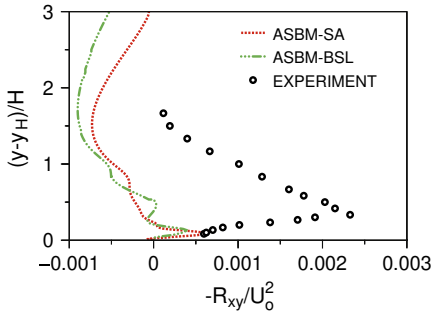

Fig. 25. Model predictions for the shear stress at the top of the hill ($x/h = 0$) for SA and ASBM-SA closure. Comparison is made to experimental values and the predictions of ASBM-BSL model.

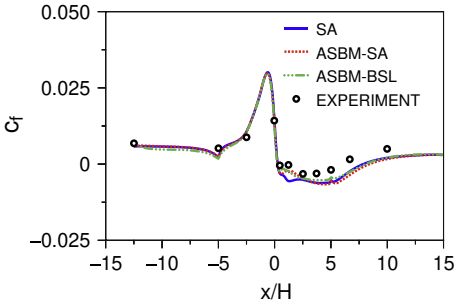

Fig. 26. SA and ASBM-SA model predictions for the skin-friction coefficient. Comparison is made to experimental values and the predictions of ASBM-BSL model.

couplings it is the one that produces the most reliable results for this case.

The computational domain and its mesh details are shown in Fig. 19. Domain dimensions are expressed in terms of the hill height H. Thus, the domain has a total height and length of $4H$ and $27.73H$, respectively, and is divided into three sections. First form left to right is the inlet section that has a length of $7.5H$ and contains $64 \times 119 \times 1$ grid cells. A second section with a length of $10H$ encloses the hill and contains $169 \times 119 \times 1$ cells, and finally the outlet block is $10.23H$ in length and contains $74 \times 119 \times 1$ cells. A grid sensitivity analysis was used in order to ensure grid independence of the solution. For this purpose, additional computations on both a coarser (with blocks of $50 \times 100 \times 1$, $120 \times 100 \times 1$ and $60 \times 100 \times 1$) and a finer grid (with blocks $97 \times 125 \times 1, 331 \times 125 \times 1$ and $158 \times 125 \times 1$) were performed. It was confirmed that the same solution was obtained when using the two finer grids, thus verifying that our solutions are grid converged.

At the inlet, the height of the cell adjacent to the wall is placed at a $y^+ \approx 0.25$. The inlet profile is extracted from a flat-plate boundary layer simulation at $\mathrm{Re}_\delta = 4772$, where the Reynolds number is based on the freestream velocity u_δ and the boundary layer thickness δ. An outflow penalty condition was used at the outlet, a no-slip condition at the bottom wall, a slip condition at the top free surface, and periodic conditions were imposed in the spanwise direction.

In the figures that follow, all quantities are normalized using the hill height H and the reference inlet freestream velocity u_δ. Measuring streamwise distance x/h from the top of the hill, profiles are extracted at four different stations inside the recirculation region (from $x/h = 1.25$ up to $x/h = 6.67$), where the most notable discrepancies between the models are expected to occur. The four stations A, B, C, and D correspond to $x/h = 1.15, 2.5, 3.75$ and 6.67 respectively.

Fig. 20 shows results for the mean streamwise velocity U_x. In all cases, comparison is made to experimental measurements and the predictions of the ASBM-BSL model. As shown, the predictions of all three closures are comparable.

Fig. 21 shows the corresponding comparison for the case of the wall-normal mean velocity, U_y. Again, the predictions of the three

Table 1
Structure scalars: auxiliary functions along shear line, $\eta_M = 1$.

$\eta_M = 1$	ϕ_1	β_1	χ_1
$\eta_f < 0$	$\frac{\eta_f - 1}{3\eta_f - 1}$	$\left[1 - b_0 \frac{\eta_f}{(1-a^2)}\left(1 + \sqrt{(a^2 - 1/3)}\right)\right]^{-1}$	$b_1\beta_1$
$0 < \eta_f < 1$	$(1 - \eta_f)$	1	$b_1 + (1 - b_1)\left[1 - \frac{(1-\eta_f)^2}{1 + b_2\eta_f/(1-a^2)}\right]$
$\eta_f > 1$	$\frac{\eta_f - 1}{3\eta_f - 1}$	$\left[1 + b_3 \frac{(\eta_f - 1)}{(1-a^2)}\eta_f\sqrt{(a^2 - 1/3)}\right]^{-1}$	$1 - \frac{(1-\beta_1)(\eta_f - 1)}{b_4(1-a^2) + (\eta_f - 1)}$

Table 2
Structure scalars: auxiliary functions along plane strain line, $\eta_M = 0$.

$\eta_M = 0$	ϕ_0	β_0	χ_0
$2\eta_f \leqslant \sqrt{3}/2$	$0.145\left[\frac{(2\eta_f)^2}{3/4} - \left(\frac{(2\eta_f)^2}{3/4}\right)^9\right]$	1	$-\left[0.342\frac{(2\eta_f)^2}{3/4} + (1 - 0.342)\left(\frac{(2\eta_f)^2}{3/4}\right)^6\right]$
$2\eta_f > \sqrt{3}/2$	$(1 + \chi_0)/3$	$-\chi_0$	$-\left[1 + b_5 \frac{(2\eta_f - \sqrt{3}/2)}{(1-a^2)} 2\eta_f\sqrt{(a^2 - 1/3)}\right]^{-1}$

closures are comparable, but overall the ASBM-SA and ASBM-BSL closures seem to provide somewhat improved predictions in the recirculation zone relative to the SA model.

Next, we compare the predictions of the ASBM-SA model for the turbulent intensities with experimental measurements and the corresponding predictions of the ASBM-BSL model. The SA model is not included in this comparison because it cannot predict the turbulent intensities. Figs. 22 and 23 show the streamwise (R_{xx}) and wall-normal (R_{yy}) Reynolds stress components respectively. In the case of R_{xx}, the ASBM-SA closure provides slightly better agreement with the experiments than the ASBM-BSL model throughout the recirculation zone. For example, at the first station A inside the recirculation region, the ASBM-SA is able to capture more satisfactorily the near-wall peak in R_{xx}, while at the last station D it slight improves the predicted R_{xx} profile. Overall, the ASBM-SA closure exhibits satisfactory agreement with experiments.

Fig. 24 shows a comparison of the shear stress predictions of ASBM-SA with the corresponding experimental measurements and the predictions of the SA and ASBM-BSL closures. In the middle of the recirculation zone (stations B and C), the hybrid closures ASBM-SA and ASBM-BSL are able to capture the peak of the shear stress more accurately than SA, but they overpredict the peak at station D, which coincides with the experimental re-attachment point. Overall, the predictions of the two hybrid closures are comparable and they are both able to capture the near-wall peak in the shear stress reasonably well. However, as shown in Fig. 25, at the top of the hill (station $x/h = 0$), we notice a problem with both model predictions, where positive magnitudes for the shear stress are predicted. These might be related to the local nature of the ASBM closure and the lack of memory effects.

Fig. 26 shows the variation of the skin-friction coefficient along the hill surface. The hybrid ASBM-SA and ASBM-BSL closures give comparable results that are in reasonable agreement with experiments. It is worth noting that in the recirculation zone, the hybrid closures are in better agreement with experiments than the SA closure.

Overall the ASBM-SA closure provides comparable or slightly improved predictions relative to the ASBM-BSL closure. On the other hand, one has to take into account that ASBM-SA is a one-equation model and as such exhibits some computational performance advantages relative to the two-equation ASBM-BSL.

5. Conclusions

A new coupling between ASBM and the SA one-equation model was presented. To implement the coupling, consistent profiles for the turbulence scales were extracted from the SA predictions and fed to ASBM through a set of algebraic expressions, applicable for a large range of turbulent flows. The ASBM-SA closure preserves (not shown here) the full realizability enjoyed by the ASBM closure and exhibits improved numerical robustness and speed of convergence relative to other couplings such as the ASBM–v^2–f and even the ASBM-BSL.

The performance of the hybrid model was evaluated in several standard benchmark cases. First, a fully-developed turbulent channel flow was considered, for which model predictions have shown satisfactory agreement with the experimental data for both mean and fluctuating quantities. Then a boundary layer simulation was performed, revealing good matching between CFD and experiment measurements for rms and shear correlations, especially for $y^+ > 10$. Then the simplest case of separated flow, that of a backward facing step, was examined. The coupled model managed to capture both peak magnitudes and freestream values of the mean and fluctuating variables, both in and out the recirculation region, exhibiting its sensitivity in anisotropic features. The ASBM-SA model was also evaluated for a case of turbulent flow in a planar asymmetric diffuser, where its predictions were found to be in fair agreement with experiments. Predictions for the static-pressure and skin-friction coefficients were within 4% of the experimental values. Finally, the model was challenged in a more difficult case involving separation, that of flow over a steep hill. Again, an overall good agreement between model and experimental predictions was achieved.

Concluding, the new coupling preserves the superior robustness of the SA closure, providing smooth converged solutions with a good convergence rate. At the same time, the hybrid closure has been able to capture effectively the turbulence anisotropy in all the flows considered as a result of the ASBM contribution. Future work will focus on testing the coupling over two-dimensional airfoil surfaces and three-dimensional smooth hills.

A Fortran-90 module containing our implementation of the ASBM is being made available online (ASBM, 2014). Researchers interested in implementing the ASBM-SA closure in their own CFD codes can contact the authors for assistance.

Acknowledgements

Support from the US Army International Technology Center and the US Air Force European Office of Aerospace Research and Development (EOARD) under Grant W911NF-11-1-0425, and from the Republic of Cyprus through the Research Promotion Foundation Project KOYΛ/Σ/0510/01 is grateful acknowledged.

The first two authors would like to thank Prof. K. Duraisami and Dr. J. O'Sullivan for fruitful discussion on the implementation of the ASBM closure.

Appendix A. Structure scalars

In addition to the description given in the introductory section of the paper, the determination of the structure scalar parameters ϕ, χ, and β is needed in order to bring the model into a closed form. This is done through a set of functions which take into account specific simplified turbulent states at the RDT limit. A specific care was given such that the model remained realizable for a wide range of mean deformations. The determination of a general turbulent state was obtained by interpolating between the target turbulent states through interpolation functions (along with model constants). The structure scalars are parameterized in terms of η_m, η_f, and a^2, representatives of the ratio of mean rotation to mean strain, frame rotation to mean strain rate, and a measure of anisotropy respectively. These in turn are defined in terms of $\hat{\Omega}_m^2$, $\hat{\Omega}_T^2$, and $\hat{S}^2$; measures of the strength of the mean rotation, total rotation, and mean strain respectively:

$$\eta_M \equiv \sqrt{\frac{\hat{\Omega}_m^2}{\hat{S}^2}}, \tag{35a}$$

$$\eta_f \equiv \eta_M - \text{sign}(X)\sqrt{\frac{\hat{\Omega}_T^2}{\hat{S}^2}}, \tag{35b}$$

$$a^2 \equiv a_{pq}a_{pq}, \tag{35c}$$

$$\hat{\Omega}_m^2 \equiv -a_{ij}\Omega_{ik}\Omega_{kj}, \tag{35d}$$

$$\hat{\Omega}_T^2 \equiv -a_{ij}\Omega_{ik}^T\Omega_{kj}^T, \tag{35e}$$

$$\hat{S}^2 \equiv a_{ij}S_{ik}S_{kj}, \tag{35f}$$

$$X \equiv a_{ij}\Omega_{ik}^T S_{kj}. \tag{35g}$$

η_M expresses the relative strength between the deformation and the rotation effects, while it conserves the material indifference property through the presence of the eddy-axis tensor a_{ij} in the invariants. for example $\eta_M = 1$ refers to pure shear flow(S), whereas $\eta_M = 0$ corresponds to purely irrotational flows, sensitized to plane strain flow(PS). Similarly, the dimensionless parameter η_f refers to rotated frames, for which the total rotation tensor is used instead of rotation tensor.

Tables 1 and 2 give the auxiliary functions for computing the structure scalars along the $\eta_M = 1$ and $\eta_M = 0$ lines respectively. The constants b_α appearing in these Tables are given by $b_0 = 1.0,\ b_1 = 0.2,\ b_2 = 3,\quad b_3 = 0.8,\ b_4 = 1.0,\ b_5 = 1.0,\quad$ and $b_6 = 0.5$.

For $\eta_M < 1$, the scalars are found by the following interpolation functions

$$\phi^* = \phi_0(\eta_f^{PS}) + \left[\phi_1(\eta_f^S) - \phi_0(\eta_f^{PS})\right]\frac{0.82\eta_M^2}{1-(1-0.82)\eta_M^2}, \tag{36a}$$

$$\chi^* = \chi_0(\eta_f^{PS}) + [\chi_1(\eta_f^S) - \chi_0(\eta_f^{PS})]\eta_M^2, \tag{36b}$$

$$\beta^* = \beta_0(\eta_f^{PS}) + [\beta_1(\eta_f^S) - \beta_0(\eta_f^{PS})]\eta_M^2. \tag{36c}$$

To completely determine the interpolation, the most appropriate values of η_f^S and η_f^{PS} have to be chosen. When $\eta_M < 1$, the possible choices for η_M are given below:

- if $\eta_f < (\eta_M - 1)\sqrt{3}/4$,
  $\eta_f^S = \eta_f - (\eta_M - 1)\sqrt{3}/4, \quad \eta_f^{PS} = \eta_f - \eta_M\sqrt{3}/4,$
- else (I) if $(\eta_M - 1)\sqrt{3}/4 < \eta_f < 0$,
  $\eta_f^S = 0, \quad \eta_f^{PS} = \eta_f/(1-\eta_M),$
- else (II) if $0 < \eta_f < \eta_M$,
  $\eta_f^S = \eta_f/\eta_M, \quad \eta_f^{PS} = 0,$
- else (III) if $\eta_M < \eta_f < \eta_M + \sqrt{3}/4(1-\eta_M)$,
  $\eta_f^S = 1, \quad \eta_f^{PS} = 1 - (1-\eta_f)/(1-\eta_M),$
- else if $\eta_f > \eta_M + \sqrt{3}/4(1-\eta_M)$,
  $\eta_f^S = 1 + \eta_f - (\eta_M + \sqrt{3}/4(1-\eta_M)),$
  $\eta_f^{PS} = \eta_f - \eta_M(1-\sqrt{3}/4).$

Otherwise, if $\eta_M > 1$, we have the following options.

- if $\eta_f < 1$,
  $\phi^* = [1/3 + (\phi_1(\eta_f) - 1/3) \times f_R],$
  $\beta^* = \beta_1(\eta_f) \times f_R, \quad \chi^* = \chi_1(\eta_f) \times f_R$
- else if $1 < \eta_f < \eta_M$,
  $\phi^* = [1/3 + (\phi_1(\eta_f = 1) - 1/3) \times f_R] \times (\eta_M - \eta_f),$
  $\beta^* = \beta_1(\eta_f = 1) \times f_R \times (\eta_M - \eta_f), \quad \chi^* = \chi_1(\eta_f = 1) \times f_R \times (\eta_M - \eta_f)$
- else if $\eta_M < \eta_f$,
  $\phi^* = [1/3 + (\phi_1(\eta_f) - 1/3) \times f_R] \times (\eta_f - \eta_M),$
  $\beta^* = \beta_1(\eta_f) \times f_R \times (\eta_f - \eta_M), \quad \chi^* = \chi_1(\eta_f) \times f_R \times (\eta_f - \eta_M)$

where $f_R = 1/(1 + 0.5(\eta_M - 1)/(1-a^2)^{5/2})$.

Finally, we need to specify the interpolation to the isotropic state for no mean deformation, where the structure scalars are chosen to be $\phi = 0$ (only vortical eddies), $\beta = 1$ (irrelevant), and $\chi = 0$ (no flattening). This is done according to:

$$\phi = \phi^* \times f_{slow}(a^2), \tag{37}$$

$$\beta = \beta^*, \tag{38}$$

$$\chi = \chi^* \times f_{slow}(a^2), \tag{39}$$

where $f_{slow}(a^2) = 0.35 f_{iso}^{5/2}(a^2) + (1-0.35)f_{iso}^{1/2}(a^2)$, and $f_{iso}(a^2) = \frac{3}{2}(a^2 - \frac{1}{3})$.

References

Alamo, J., Jimenez, J., 2003. Spectra of very large anisotropic scales in turbulent channels. Phys. Fluids 15, L41.

ASBM, 2014. The Code Will be Uploaded Soon in our Group's Website. <http://ucy-compsci.org>.

Aupoix, B., Kassinos, S., Langer, C., 2009. ASBM-BSL: an easy access to the structure based model technology. In: Sixth International Symposium on Turbulence and Shear Flow Phenomena, Seoul-Korea, June 22–24.

Benton, J., 2011. Evaluation of v^2-f and ASBM Turbulence Models for Transonic Aerofoil RAE2822. Progress in Wall Turbulence: Understanding and Modelling, ERCOFTAC Series. pp. 439–450.

Bradshaw, P., Ferriss, D., Atwell, N., 1967. Calculation of boundary layer development using the turbulent energy equation. J. Fluid Mech. 28 (3), 593–616.

Buice, C., Eaton, J., 2000. Experimental investigation of flow through an asymmetric plane diffuser. J. Fluids Eng. 122, 433–435.

DalBello, T., Dippold, V., Georgiadis, N., 2005. Computational Study of Separating Flow in a Planar Subsonic Diffuser. Tech. Mem. 213894. NASA.

Dryden, H.L., 1948. Recent advances in the mechanics of boundary layer flow. In: Mises, R.V., Karman, T.V. (Eds.), Advances in Applied Mechanics, vol. 1, pp. 1–40.

Fares, E., Schroder, W., 2005. A general one-equation turbulence model for free shear and wall-bounded flows. Flow Turbul. Combust. 73, 187–215.

Haire, S., Reynolds, W., 2003. Toward an Affordable Two-Equation Structure-Based Turbulence Model. Technical Report TF-84. Thermosciences Division Department of Mechanical Engineering Stanford University, California 94305.

Ham, F., Mattson, K., Iaccarino, G., 2006. Accurate and Stable Finite Volume Operators for Unstructured Flow Solvers. Annual Research Briefs, Center for Turbulence Research. pp. 243–261.

Hoyas, S., Jimenez, J., 2006. Scaling of the velocity fluctuations in turbulent channels up to $Re_\tau = 2003$. Phys. Fluids 18, 011702.

Jovic, S., Driver, D., 1995. Reynolds number effects on the skin friction in separated flows behind a backward facing step. Exp. Fluids 18, 464–467.

Kalitzin, G., Iacarrino, G., Langer, C., Kassinos, S., 2004. Combining Eddy-Viscosity Models and the Algebraic Structure-Based Reynolds Stress Closure. Annual Research Briefs, Center for Turbulence Research. pp. 171–182.

Kaltenbach, H., Fatica, M., Mittal, R., Lund, T., Moin, P., 1999. Study of flow in a planar asymmetric diffuser using large-eddy simulation. J. Fluid Mech. 390, 151–185.

Kassinos, K., Reynolds, W., 1994. A structure-Based Model for the Rapid Distortion of Homogeneous Turbulence. Technical Report TF-61. Thermosciences Division Department of Mechanical Engineering Stanford, California 94305.

Kassinos, S., Langer, C., Haire, S., Reynolds, W., 2000. Structure-based turbulence modeling for wall-bounded flows. Int. J. Heat Fluid 21, 599–605.

Kassinos, S., Reynolds, W., Rogers, M., 2001. One-point turbulence structure tensors. J. Fluid Mech. 428, 213–248.

Kassinos, S., Langer, C., Kalitzin, G., Iaccarino, G., 2006. A simplified structure-based model using standard turbulence scale equations: computation of rotating wall-bounded flows. Int. J. Heat Fluid 27, 653–660.

Langer, C., Reynolds, W., 2003. A New Algebraic Structure-Based Turbulence Model for Rotating Wall-Bounded Flows. Technical Report TF-85. Thermosciences Division Department of Mechanical Engineering Stanford, California 94305.

Le, H., Moin, P., Kim, J., 1997. Direct numerical simulation of turbulent flow over a backward-facing step. J. Fluid Mech. 330, 349–374.

Lien, F., Kalitzin, G., Durbin, P., 1998. RANS Modelling for Compressible and Transitional Flows. Annual Research Briefs, Center for Turbulence Research. pp. 267–286.

Loureiro, J., Pinho, F., Silva, F., 2007. Near wall characterization of the flow over a two-dimensional steep smooth hill. Exp. Fluids 42 (3), 441–457.

Nagano, Y., Pei, C., Hattori, H., 2000. A new low-Reynolds number one-equation model of turbulence. Flow Turbul. Combust. 63, 135–151.

Patel, V., Rodi, W., Scheuerer, G., 1985. Turbulence models for near-wall and low Reynolds number flow: a review. AIAA J. 23, 1308–1319.

Poroseva, S., Kassinos, S., Langer, C., Reynolds, W., 2002. Structure-based turbulence model: application to a rotating pipe flow. Phys. Fluids 14, 1523–1532.

Rahman, M., Siikonen, T., Agarwal, R., 2011. Improved low Re-number one-equation turbulence model. AIAA J. 49 (4), 735–747.

Reynolds, W., Langer, C., Kassinos, S., 2002. Structure and scales in turbulence modeling. Phys. Fluids 14, 2485–2492.

Rodi, W., 1976. A new algebraic relation for calculating the Reynolds stress. Z. Angew. Math. Mech., 56.

Spalart, P., Allmaras, S., 1994. A one-equation turbulence model for aerodynamic flows. Rech. Aerospatiale 1, 5–21.